Journal of Alloys and Compounds 1070 (2026) 188680

Contents lists available at ScienceDirect

Journal of Alloys and Compounds

journal homepage: www.elsevier.com/locate/jalcom

Complex N-phase in the Al–Fe–Pt alloy system

Yael Tamir [a], Alexander Upcher [b], Benjamin Grushko [c], Louisa Meshi [a,*]

[a] Department of Materials Engineering, Ben Gurion University of the Negev, Beer Sheva, Israel
[b] Ilse Katz Institute for Nanoscale Science and Technology, Ben Gurion University of the Negev, Beer Sheva, Israel
[c] ERC-1, Forschungszentrum Jülich, Jülich 52425, Germany

ARTICLE INFO

Keywords:
Al–Fe–Pt
Intermetallics
Electron diffraction
High-angle annular dark-field imaging

ABSTRACT

New, so-called, N-phase revealed around ~$Al_{79}Fe_{12}Pt_9$ (B. Grushko, J. Alloys Comp. 829 (2020) 154444) has been studied by 3D electron diffraction and high-angle annular dark-field imaging. Its structure is concluded to be monoclinic with the cell parameters of $a \approx 1.243$ nm, $b \approx 1.654$ nm, $c \approx 1.97$ nm and $\beta \approx 107.24°$. The symmetry of the unit cell can be described by either $P2_1$ (No. 4) or $P2_1/m$ (No. 11) space groups. Despite extensive study, the structure solution of the N-phase was impeded by abundant structural defects. Electron diffraction data point to a close structural relation between the Al–Fe–Pt N-phase and the E-phases earlier observed in the Al–Ru–Rh or Al–Co–Rh(Ir) alloy systems. Both the N-phase and E-phases have very similar values of the b and c cell parameters while their cell parameters a are related as $a_N \approx a_E/[2\sin(2\pi/5)]$. The monoclinic Al–Fe–Pt N phase is established as a distinct member of the pseudo-decagonal intermetallic family.

1. Introduction

An investigation of the Al–Fe–Pt alloy system [1] revealed a new phase forming at 700–850 °C around ~$Al_{79}Fe_{12}Pt_9$. In [1], its powder XRD pattern (see below in more detail) could not be indexed or associated with any known phase. On one hand, the distribution of the strongest reflections was quite typical of the phases exhibiting pseudo-decagonal structures (see Ref. [2–5], for example), on the other hand, it also showed noticeable differences, as was illustrated in Fig. 4 of Ref. [6].

The corresponding Al–Fe–Pt phase was designated N keeping in mind its quite close equivalent composition to that of the orthorhombic Al–Fe–Pd N-phase reported in Ref. [7], in addition to the fact that Pd and Pt belong to the same column of the Periodic Table. The Al–Fe–Pd N-phase forming around $Al_{76.5}Pd_{10.5}Fe_{13.0}$ was studied by electron diffraction and found to be orthorhombic with the cell parameters $a \approx 2.31$ nm, $b \approx 1.60$ nm and $c \approx 4.70$ nm, the reflection conditions were consistent with a B-centered structure.

As follows from the present study, the new Pt-containing phase has a monoclinic structure with indeed similar cell parameter b but very different cell parameters c and a. In order to discriminate these rather different structures the corresponding Al–Fe–Pt phase is designated below by the italic symbol N-phase.

In this contribution the Al–Fe–Pt N-phase is studied in more detail by electron diffraction and high-resolution electron microscopy.

2. Experimental

The alloy of the nominal composition of $Al_{79.1}Fe_{12.5}Pt_{8.4}$, was prepared and preliminary studied in Ref. [1]. It was produced by levitation induction melting in a water-cooled copper crucible under a pure Ar atmosphere. The purity of Al was 99.999%, of Fe 99.99%, of Pt 99.9%. The sample used for the structural determination was annealed at 850 °C under vacuum for 284 h. The annealed sample was examined in [1] by Scanning Electron Microscopy (SEM) and Powder X-ray Diffraction (XRD). The local compositions were measured by Energy-Dispersive X-ray Analysis (EDX) in SEM on polished unetched surfaces using a JEOL 840a scanning electron microscope equipped with EDAX Genesis 200 emission spectroscopy system. Powder XRD examinations were carried out using Cu Kα1 radiation and an imaging plate (Huber G670).

For the Transmission Electron Microscopy (TEM) analysis, the parts of the above-mentioned annealed sample were ground into powder using an agate mortar and pestle, dispersed in isopropanol and stirred in an ultrasonic bath. This suspension was dropped on a carbon-coated Cu TEM grid for subsequent Electron Crystallography (EC) study. The N-phase particles were identified using EDS in TEM. Structure characterization was performed using 3 Dimensional Electron Diffraction Tomography (3D ED) method [8–10]. The investigation was carried out

---

* Corresponding author.
E-mail address: louisa@bgu.ac.il (L. Meshi).

https://doi.org/10.1016/j.jallcom.2026.188680
Received 8 March 2026; Received in revised form 14 May 2026; Accepted 15 May 2026
Available online 16 May 2026
0925-8388/© 2026 The Author(s). Published by Elsevier B.V. This is an open access article under the CC BY license (http://creativecommons.org/licenses/by/4.0/).

using JEOL 2100 TEM operated in 200 kV using high-tilt tomography holder. Multiple electron diffraction datasets were recorded manually from different particles using the Selected Area Electron Diffraction (SAED) mode, with a constant tilt step of 1° at angular range from ±25° to ±58° and a precession angle of 1°. Precession was added to improve the resolution of the data and eliminate the missing wedge between the consecutive frames [11–14]. Initial data processing and structure characterization was carried out using PETS software [15]. High Resolution TEM (HRTEM) investigations were performed on a JEOL JEM-2100F TEM operating at 200 kV equipped with JED-2300T EDS, scanning coils and GATAN 806 High-Angle Annular Dark Field (HAADF) detector. For (S)TEM analysis, Spectra 200 (Thermo Fisher Scientific) scanning transmission electron microscope (S/TEM) equipped with a probe Cs-corrector (S-CORR) and cold-FEG electron source at an accelerating voltage of 200 kV was used. In STEM mode, the images were recorded with high-angle annular dark field (HAADF) detector.

3. Results and discussion

3.1. *Characterization of the structure of the N-phase using electron crystallography*

For structure characterization, several particles of the *N*-phase were examined. First, chemical analysis was performed on each studied particle (using EDS) to ensure their composition was close to $Al_{80}Fe_{12}Pt_8$. Then, using 3D ED technique [8–10] we acquired the diffraction data and determined the cell geometry of the *N* phase. A series of off-axis patterns with large angular separations were recorded; see Table 1 summarizing the acquired datasets. Data processing and subsequent structure determination were carried out using PETS software [15] from each dataset independently. Final average composition of the particles was approximately $Al_{79}Fe_{13}Pt_8$. The structure was found to be monoclinic with the average cell parameters $a \cong 1.24 \pm 0.01$ nm, $b \cong 1.654 \pm 0.025$ nm, $c \cong 1.97 \pm 0.04$ nm and $\beta \cong 107.24 \pm 0.6^\circ$. A successful indexing of all observed electron diffraction patterns was achieved using these unit cell parameters. The corresponding precession electron diffraction (PED) patterns of the *N*-phase along the [010] and [100] directions are shown in Fig. 1. The [010] electron diffraction pattern, Fig. 1a, exhibits pseudo-tenfold symmetry with strong reflections arrange in pseudo-decagonal rings which is characteristic of pseudo-decagonal structures [7,16–18].

It should be noted that the standard deviation of the estimated cell parameters is higher than commonly accepted for the structures determined using electron crystallography methods. Therefore, we suggest that each studied particle had its distinct stoichiometry and exhibited somewhat different cell parameters, which points to a high degree of atomic substitution that might hinder structure solution.

Fig. 2 shows a linear trend with $R^2 \approx 0.7$ (where R^2 is the measure of goodness of fit used in linear regression [19]), between the cell parameter *b* (as an example) and the Fe-to-Pt ratio, indicating a moderate correlation between composition and the *b* cell parameter. The observed trend is consistent with Vegard's law, which describes an approximately linear relationship between cell parameters and composition at constant temperature [20].

The reciprocal lattice cuts of a dataset taken from one of the particles are shown in Fig. 3. The reflections with the odd values of *k* are absent in the $(0kl)^*$ and $(hk0)^*$ planes, but not in other reciprocal lattice planes, like $(1kl)^*$, $(hk1)^*$ and $(h1l)^*$. From these observations, the serial reflection condition $0k0$: $k = 2n$ is obtained, suggesting the presence of a twofold screw axis parallel to the *b*-axis of the crystal. Therefore, according to the International Tables of Crystallography [21], only $P2_1$ (No. 4) and $P2_1/m$ (No. 11) space groups can describe the symmetry of this unit cell. The two space groups differ in whether an inversion center is present.

The HAADF images of the *N*-phase taken along the [010] direction (Fig. 4a) provided additional information. In HAADF images, the contrast is dictated by the atomic number of elements [22,23], namely, the columns containing the heavy atoms appear in the image as bright spots. The strongest intensity of these spots is expected to originate from the Pt atoms, moderate intensity from Fe, while the columns consisting solely of Al atoms will appear the darkest and may be difficult to discern. Considering that different layers within the same column may be occupied by different elements, and only the averaged total scattering is observed, it is not possible to directly assign a specific column to a specific element, even though the elements exhibit significantly different scattering strengths.

As can be seen, the brightest spots, originating from the Pt/Fe containing columns, belong to the corners of the parallelepipeds in the images. The following description is related to the two-dimensional projection of an "idealized" structure, with the corresponding terminology implying three-dimensional distribution of atoms. Thus, each corner is surrounded by decagonal rings of heavy atoms, which are probably arranged in two sets of pentagons rotated by 36° and shifted along the *b* axis. This is logical, considering the distribution of other heavy atoms at the corners of other pentagons, as is shown in Fig. 4b. Subsequently, the "atoms" in different layers are shown in Fig. 4b by different colors. Apart from the completely decorated pentagons, there are also partially decorated pentagons shown by broken lines.

The dimension of the pentagons ($s = 0.47$ nm, the diagonal of the pentagon is τ times longer) is the same as in the E-phase (see Ref. [3–5] and references therein) and many other Al–TM structures (see more below). Subsequently, following geometrical considerations, the ideal cell parameters of *N* are: $a = s(1+\tau) = 1.230$ nm, $c = s(1+2\tau) = 1.99$ nm and $\beta = 108^\circ$, i.e. close to those experimentally observed. In the tiling of the HAADF image in Fig. 4b, each "blue" pentagon is decorated by heavy atoms (atom columns) in its corners and in its center. In the pentagons, adjusted to the corners of the unit cell (shown by broken lines), two atoms in one of the diagonals are missing. Subsequently, three kinds of tiles building the pattern can be asserted, as is described in Fig. 4c. In addition to the pentagons, there are rhombi filling the gaps between the pentagons and containing two additional heavier atoms, marked in orange in Fig. 4b.

As can be seen in Fig. 5, each corner of the unit cell is surrounded by a ring of ten above-mentioned pentagons, and the "yellow pentagons" with alternating orientations are arranged into "belts". The corresponding "red" decagons share their sides along the *c*-direction and intersect along the *a*-directions.

The structure can be described in an unconventional setting of the

Table 1
Summarized data table containing EDS results and cell parameters as processed in PETS software.

Data Set	EDS results			Cell parameters				Indexed reflections	Completeness
	Al at%	Fe at%	Pt at%	*a*, nm	*b*, nm	*c*, nm	*β*,°	%	%
1	78.31	12.87	8.82	1.2516	1.6832	1.9632	105.752	99.69	56.38
2	81.08	11.51	7.41	1.2131	1.6855	2.0689	107.866	74.40	46.75
3	79.08	12.56	8.37	1.2452	1.6606	1.9833	106.534	85.71	48.1
4	79.82	12.19	7.99	1.2103	1.6766	1.9649	106.253	68.31	29.74
5	80.30	11.40	8.30	1.2480	1.6350	1.9775	106.974	90.25	59.87
6	80.17	12.27	7.56	1.2508	1.6895	1.9656	105.853	97.66	55.18

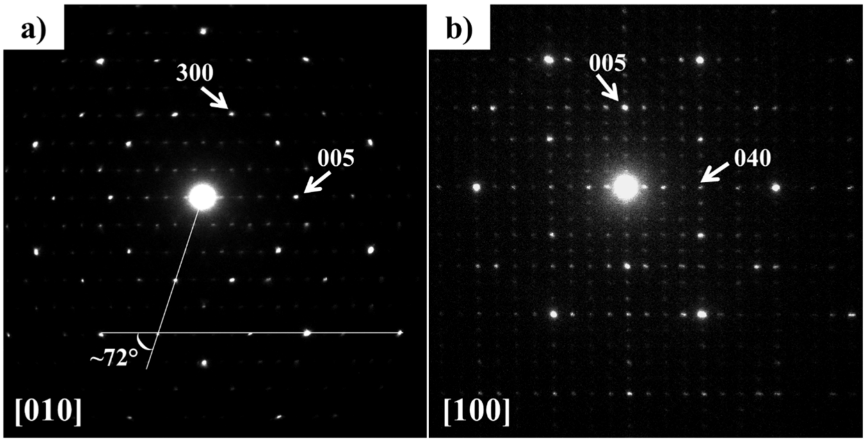

Fig. 1. PED patterns taken from the *N*-phase structure along: (a) [010] and (b) [100] orientations.

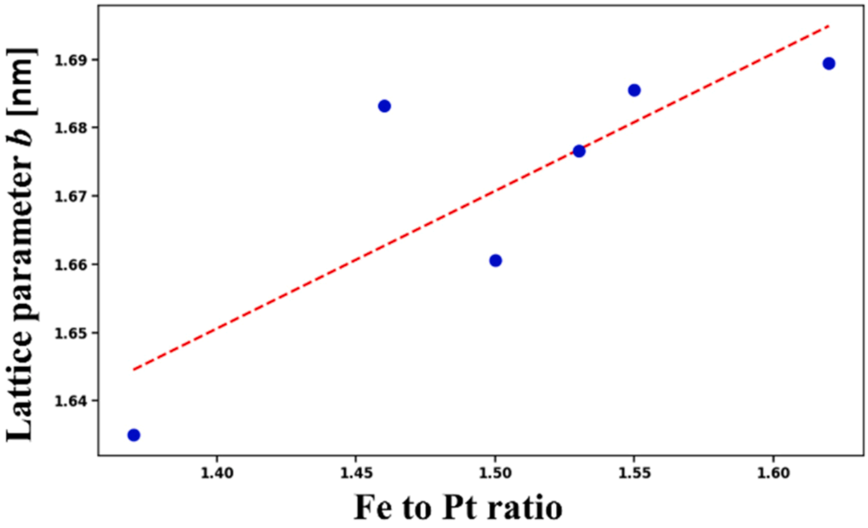

Fig. 2. Dependence of the *b* cell parameter value on Fe/Pt ratio.

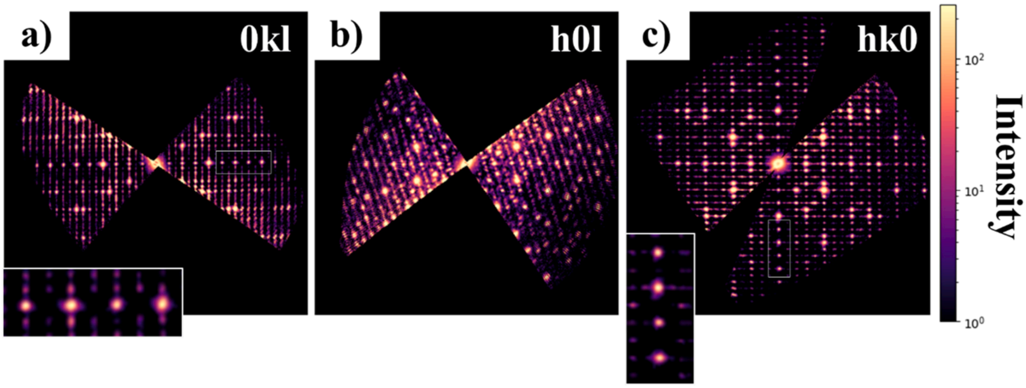

Fig. 3. Reconstructed 0*kl*, *h*0*l* and *hk*0 sections of the reciprocal space taken from the 3D ED data captured from the $Al_{79}Fe_{13}Pt_8$ *N*-phase. The intensity of reflections is presented in logarithmic scale. Inserts are added to emphasize the lack of the odd 0*k*0 reflections at the 0*kl* and *hk*0 sections.

space group, $B2_1$ or $B2_1/m$, that, as shown in the Appendix, facilitates a comparison with the N-phase of Al-Fe-Pd. The unconventional setting is obtained by the transformation **a**, **b**, **a**+ 2**c**, which leads to the *B*-centered unit cell shown in Fig. 5, for which $c_B = 2c_P\sin\left(\frac{2\pi}{5}\right) = 3.785nm$.

Despite numerous attempts to determine the atomic model of the *N*-phase using 3D ED (either independent or merged datasets), the result was still negative. Both direct methods (as implemented in SIR2019 [24]) and the charge flipping algorithm (Jana [25]) were tested. The analysis of the datasets (including merged ones) revealed a negative slope in the Wilson plots and very noisy data. It is customary to attribute

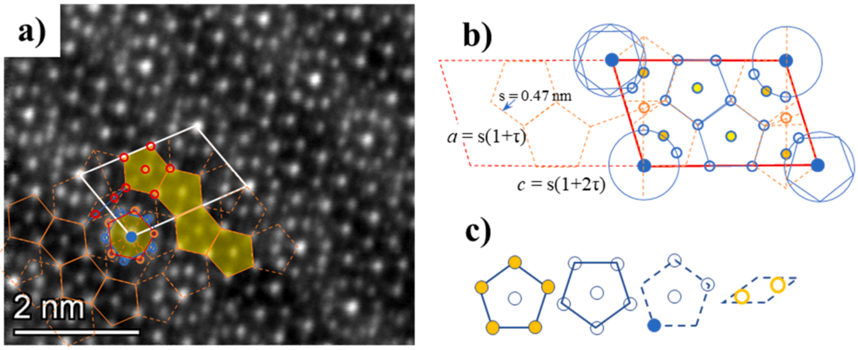

Fig. 4. HAADF image of the *N*-phase taken along the [010] zone axis (a) and its "idealized" tiling by pentagons of 0.47 nm edge length (b). Three differently decorated pentagonal tiles and a rhombic tile are shown in (c).

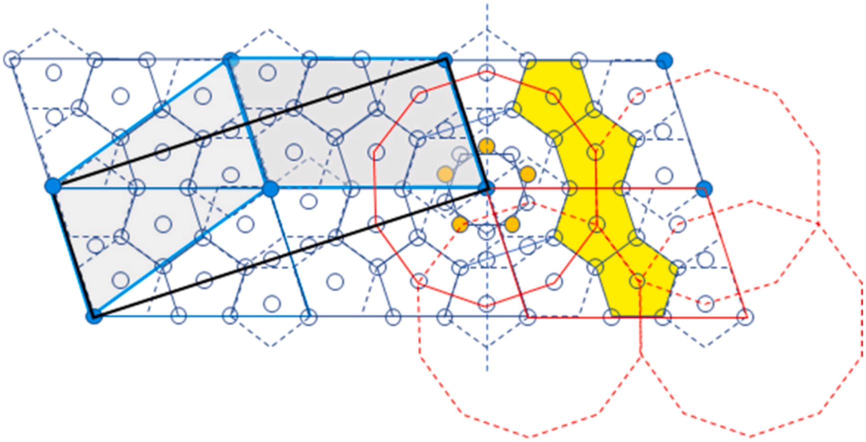

Fig. 5. Tiling of the *N*-phase by decagonal rings (columns).

these effects to dynamical scattering; however, the sample thickness does not appear to be excessively high. Indeed, the above-mentioned high-quality HAADF images were obtained from the same particles. On the other hand, the regions of a regular structure, as in Fig. 4a, were quite small, and high densities of structural defects were revealed within each particle (see Fig. 6). Such defects strongly influenced the measured intensities of the electron diffraction reflections.

Thus, in Fig. 6a, the local atomic packing, indicated by arrows, shows a stacking fault and a boundary (presumably a twin boundary). Some grains contained multiple domains arranged in a maze-like pattern (Fig. 6b). These grains exhibited various structural defects.

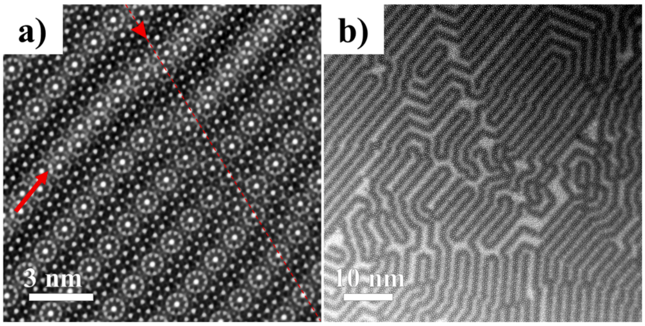

Fig. 6. HAADF images taken along the [010] zone axis of the $Al_{79}Fe_{13}Pt_8$ particles. Arrow point on stacking fault in (a), while twin boundary is shown by dashed line and arrowhead.

3.2. *N*-phase vs. E-phase

In agreement with the powder XRD examinations, mentioned in the Introduction section, both present electron diffraction and HAADF data point to a close structural relation of the Al–Fe–Pt *N*-phase to the E-phase forming in closely equivalent compositional ranges of the neighboring ternary Al–TM alloy systems (see Fig. 4 of Ref. [6]) and extensively studied earlier in Al–Ru–Rh system in Ref. [3–5].

For comparison, the HRTEM image of the E-phase along the [010] direction is shown in Fig. 7a together with the corresponding tiling by the decagonal rings (Fig. 7b). The E-phase is orthorhombic with the cell parameters of $a \approx 2.31$ nm, $b \approx 1.60$ nm and $c \approx 2.00$ nm. Thus, both the *N*-phase and E-phases have very similar values of the *b* and *c* cell parameters, while their cell parameters *a* are related as $a_N \approx a_E/2\sin(2\pi/5)$ as can be easily concluded from the description in Fig. 7b. The volume of the "ideal" unit cell of the *N*-phase is exactly half of that of the E-phase.

Along with the overall similarity, some differences in the distribution of heavy elements in E and *N* phases can be observed in Fig. 7e. In *N*, the heavy elements are located at the corners of the 'blue' pentagons, whereas in the E-structure they occupy both the corner and mid-edge positions of the decagonal rings.

3.3. Suggested phase transition

The above-mentioned defect structure of the *N*-phase might be a result of a phase transformation from an initial state forming by solidification. The as-cast structure of the relevant alloy has not been studied in Ref. [1], but it is plausible to suggest the formation of a quasiperiodic decagonal phase in as-cast material, subsequently annealed in the

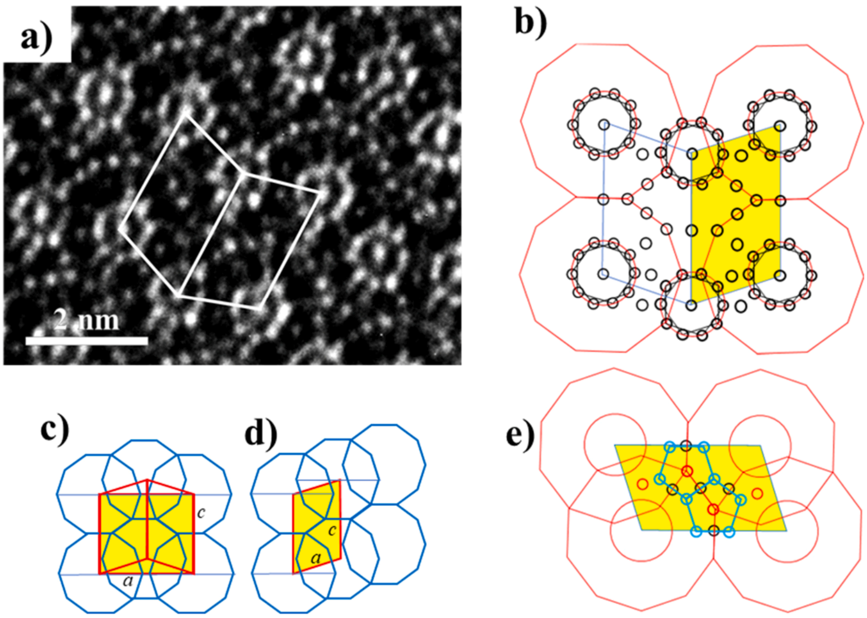

Fig. 7. HAADF image of the Al–Rh–Ru E-phase (a) and the geometry of its tiling by decagonal rings (b); the simplified presentation of the E-phase (c) is compared to that of the *N*-phase (d). In (e) the atomic columns whose locations are the same in E and *N* are shown red (including those schematically shown by rings in the corners of the unit cell), those in E are black and those in *N* are blue.

present investigation. Indeed, more recently, quite similar powder XRD pattern has been revealed in an Al–Fe–Ir sample of a closely equivalent composition of $Al_{77.5}Fe_{7.2}Ir_{15.3}$, annealed also at 850 °C [6]. On the other hand, an independent recent investigation of an $Al_{79}Fe_5Ir_{16}$ sample annealed at somewhat higher 927 °C [26] revealed a stable decagonal structure with the 1.6 nm periodicity in the specific direction (D_4). In addition to the powder XRD examination, (reproduced from [26] in Fig. 8 and compared to the powder XRD patterns of the N-phases) this finding was confirmed there by electron diffraction. The composition studied in [26] is close to the Ir-rich limit of the N-phase compositional range reported in Ref. [6].

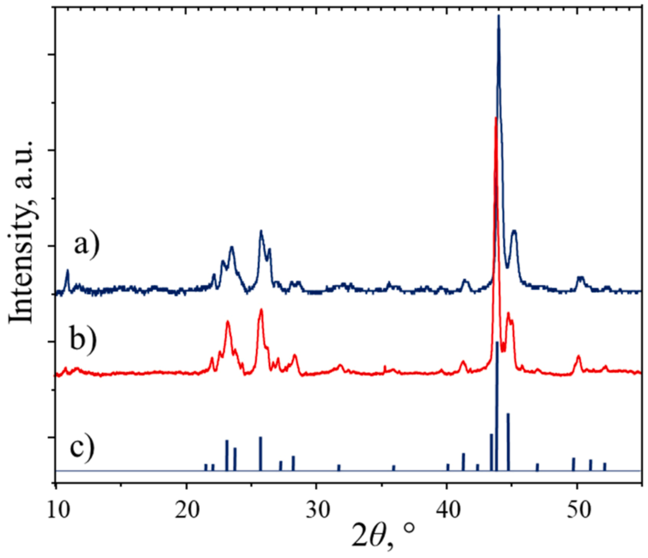

Fig. 8. Powder XRD patterns of: a) $Al_{79}Fe_{12}Pt_9$ annealed at 850 °C for 284 h [1], b) $Al_{77.5}Fe_{6.5}Ir_{16}$ annealed at 850 °C for 404 h [6], and c) the positions and intensities of the diffraction lines of $Al_{79}Fe_5Ir_{16}$ annealed at 927 °C for 140 h (redrawn from Ref. [26] where the corresponding pattern was indexed as belonging to a quasicrystalline D_4-phase). The nominal compositions of the alloys are given.

The observations reported in Ref. [6] and Ref. [26] are not in direct contradiction, as the different structures were identified in samples with slightly different compositions and annealed at different temperatures. As demonstrated in Ref. [2], both periodic and quasiperiodic pseudo-decagonal structures can be formed even at identical compositions when annealed at different temperatures. Conversely, quasiperiodic and complex periodic structures have also been found to coexist at the same temperature, although their compositions differed slightly (see, for example, Ref. [27,28]).

In Ref. [6], a sample of the corresponding nominal composition was also examined after annealing at 1100 °C. However, due to a slight deviation of its actual composition, the sample contained a major neighboring phase, which prevented identification of the minor phase(s) in the powder XRD pattern. In contrast, the Al–Fe–Pt *N*-phase observed at 700–850 °C does not appear in the 1100 °C isothermal section reported in Ref. [1].

It is worth noting the observations of the initial stages of formation of the $Al_{77}Rh_{15}Ru_8$ decagonal phase, shown in Fig. 2 of Ref. [4]. In that study, the electron diffraction pattern exhibited pseudo-decagonal symmetry with characteristic "triangle" spots and reflection splitting. This state was associated with an incomplete transformation of the decagonal phase forming in the solidified material.

3.4. *Minor phases revealed by TEM*

The abundance of the above-mentioned structural defects of the major *N*-phase is not the only indication of an incomplete transformation of solidified material. During the investigation of the *N*-phase, some particles exhibited a different structure. Analyses of the corresponding 3D ED datasets indicated an orthorhombic structure with the cell parameters $a = 1.23$ nm, $b = 1.61$ nm, and $c = 2.32$ nm, typical of the ε_6-phase forming in the system at somewhat lower Al content [1]. The corresponding reciprocal lattice cuts (Fig. 9) exhibited the following reflection conditions: ($0kl$): $l = 2$ n, ($hk0$): $h+k = 2$ n, ($h00$): $h = 2$ n, ($0k0$): $k = 2$ n, and ($00l$): $l = 2$ n, which correspond to the diffraction symbol *Pc_n* [21]. In agreement with other ε_6 structures, *Pcmn* (No. 62) was assigned as the space group. Reflections of this phase were not visible in the corresponding powder XRD patterns due to a negligible fraction of this phase in the alloy. Although the ε_6-phase belongs to the

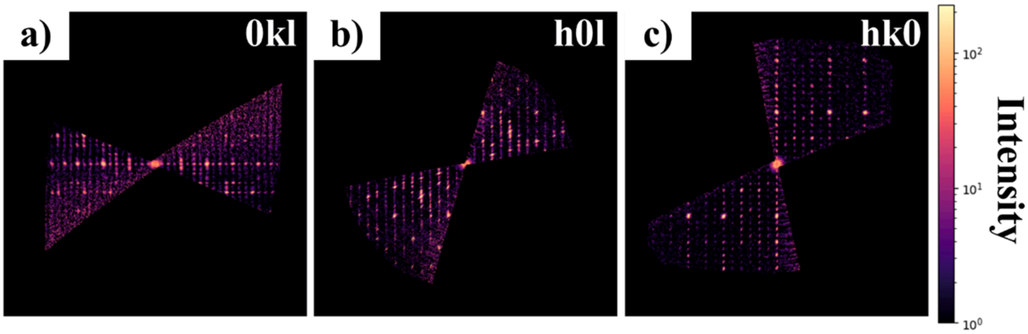

Fig. 9. 3D ED reciprocal lattice cuts of ε_6 presented in logarithmic scale.

Al–Fe–Pt system, it is not in equilibrium with the *N*-phase at 800 °C, as was established in Ref. [1]. Alternatively, it could remain untransformed during annealing of solidified materials. The composition of the ε_6-phase measured in TEM was consistent with that reported in Ref. [1].

The binary ε_6-phase structure has been reported to exist in the Al–Pd and Al–Rh alloy systems and as a ternary phase in several Al–TM1-TM2 alloy systems (1 and 2 referring to different transition metals) and its structure was extensively studied (see [29] and references therein).

Another structure was observed at the periphery of a particle containing the major *N*-phase (see the HRTEM image in Fig. 10a). In contrast to the above-mentioned decagonal tiling characteristic of the *N*-phase, this region can be tiled by flattened hexagons decorated with pentagonal motifs at their corners (Fig. 10b). Although the *b* cell parameter could not be determined from this particular orientation, it is likely to be approximately ~1.6 nm, similar to the ε_6, *N*, and E phases. Such a tiling pattern characteristic of the so-called ξ-phase, which is structurally related to the ε_6-phase mentioned above. The estimated cell parameters of what appears to be an orthorhombic ξ-type structure are: $a_\xi \approx 1.97$ nm and $c_\xi \approx 1.43$ nm.

Both the ξ-phase and ε_6-phase are constructed from pentagons with ~0.47 nm edges, arranged at the corners of flattened hexagons - features that are clearly recognizable in Fig. 10a. However, in the ξ-phase the flattened hexagons are aligned parallel to one another, whereas in ε_6 they are arranged in a herring-bone pattern (see Fig. 10c). Consequently, the cell parameters *c* and *a* of the 'ideal' ξ and ε_6 phases are related by the golden mean τ as follows: $a_\xi = \tau c_\varepsilon$ and $c_\xi = a_\varepsilon / \tau$.

Although the ξ-phase belongs to the binary Al–Pt alloy system [1], its extension toward the relevant ternary compositions seems unlikely, considering the formation of several other phases in between (see the isothermal sections in Ref. [1]). Alternatively, it may be metastable, like the ξ-type structures observed in solidified Al–Pd–Mn alloys, where they coexist with the stable ε_6-phase (see, for example, Ref. [30]). Since the *N*-phase forms upon annealing, intermediate structural states are possible, particularly through the formation of ξ-type layers. Indeed, the ξ-phase and the *N*-phase have very similar cell parameters, with $a_\xi \approx c_N$. Therefore, the ξ-phase could also act as an intermediate buffer between the *N* and the ε_6 phases.

4. Summary and conclusions

Electron crystallography-based analysis established that the Al–Fe–Pt *N*-phase is a monoclinic pseudo-decagonal intermetallic with average cell parameters $a \approx 1.24$ nm, $b \approx 1.65$ nm, $c \approx 1.97$ nm, and $\beta \approx 107°$. Although all diffraction data could be indexed within this unit cell (using space group $P2_1/m$), significant variability in cell parameters indicated a high degree of atomic substitution, pointing to a variability of the parameters as a function of the composition. Furthermore, the substantial density of structural defects along with the above stated variations in lattice constants ultimately prevented successful solution of the atomic model. HAADF-STEM imaging revealed characteristic tiling

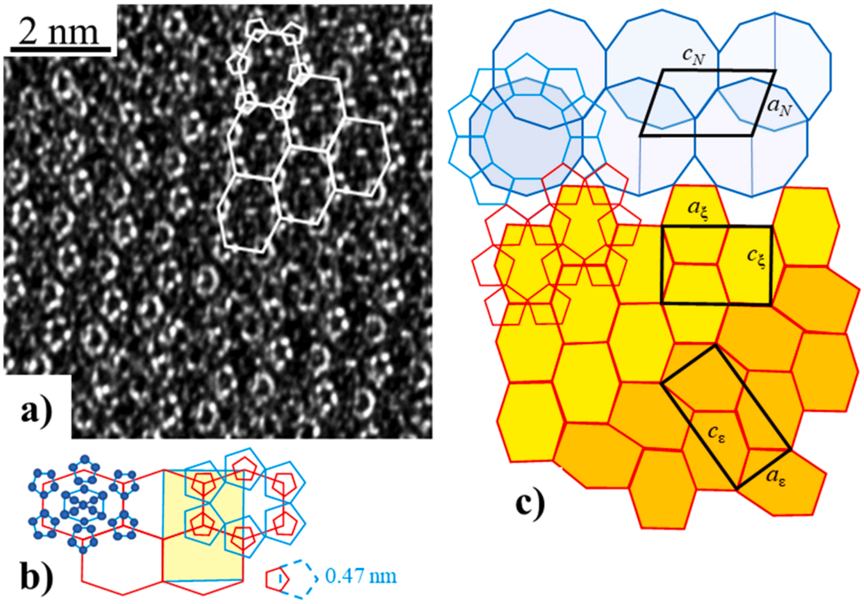

Fig. 10. HRTEM image of a minor phase and its tiling with flattened hexagons (a). Schematic "decoration" of a single tile (b) and a possible model of epitaxy of suggested ξ and ε_6 on the *N*- phase (c).

by heavy-atom-decorated pentagons forming decagonal rings, consistent with pseudo-decagonal motifs observed in related Al-transition-metal phases.

A close structural correspondence between the *N*-phase and the orthorhombic E-phase was confirmed, particularly in their *b* and *c* cell parameters and in their heavy-atom tiling patterns, although distinct differences in the decoration of decagonal rings were identified. These similarities, together with the abundance of structural defects, suggest that the *N*-phase forms through solid-state transformations of an initially quasiperiodic decagonal phase, consistent with phase relations reported in related Al-TM systems.

In addition to the major *N*-phase, TEM revealed minor inclusions of the ε_6 and a ξ-type phases. Both phases display tiling built from pentagonal units with ~0.47 nm edges and exhibit cell parameters related to those of the *N*-phase through simple τ-scaling relationships. The ξ domains were typically located at particle peripheries and may represent metastable remnants or intermediates formed during the transformation sequence from a quasiperiodic precursor toward the *N*-phase. Their geometric compatibility with both *N* and ε_6 suggests that ξ-like layers could act as structural buffers during phase evolution.

Overall, the results identify the *N*-phase as a distinct member of the pseudo-decagonal family of Al–TM intermetallics, structurally linked to the E- and ε_6-phases and likely formed through a multistep transformation pathway involving quasiperiodic precursors and intermediate complex structures.

CRediT authorship contribution statement

Benjamin Grushko: Writing – review & editing, Methodology, Investigation, Funding acquisition, Data curation, Conceptualization. **Alexander Upcher:** Investigation, Formal analysis. **Louisa Meshi:** Writing – review & editing, Validation, Supervision, Resources, Methodology, Funding acquisition, Conceptualization. **Yael Tamir:** Writing – original draft, Visualization, Investigation, Formal analysis.

Declaration of Competing Interest

The authors declare that they have no known competing financial interests or personal relationships that could have appeared to influence the work reported in this paper.

Acknowledgements

We would like to thank Dr. Susanna Syniakina (BGU) for her technical support throughout this study.

Appendix

It is worthwhile to compare the tiling of the Al–Fe–Pt *N*-phase with that of the above-mentioned orthorhombic Al–Fe–Pd N-phase [7]. For this purpose, a common coordinate system, corresponding to the *B*-centered orthorhombic unit cell of the latter, and the *B*-centered pseudo-orthorhombic unit cell of the former, introduced in Section 3.1, is appropriate. Essentially, both structures show some similarities in projections along the *b*-axis (see Fig. 11). In both cases, the projections can be described by arrangements of four decagonal rings of small pentagons (s = 0.47 nm) located near the corners of the rectangular unit cell projections, along with an additional decagonal ring at the center.

In contrast, in the Al–Fe–Pd N-phase the decagonal rings neither touch nor intersect. Instead, they are connected by elongated hexagons. Each hexagon connects the centers of six small pentagons originating from three adjacent rings (highlighted in orange in Fig. 11b), in a manner similar to that observed in the structure of the $Al_{13}Fe_4$ phase (see, for example, Ref. [31]).

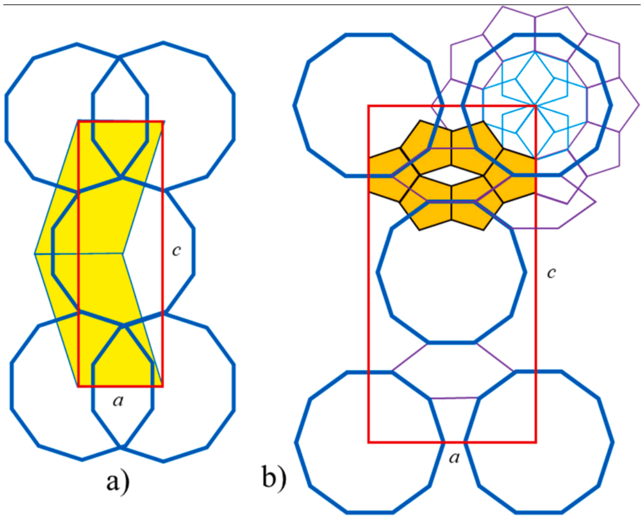

Fig. 11. Comparison of the tiling geometries of the *b*-projections of unit cells of the Al–Fe-Pt *N*-phase (a) and of the Al–Fe-–Pd N-phase [7] (b)

References

[1] B. Grushko, A study of the Al–Fe–Pt alloy system, J. Alloy. Compd. 829 (2020) 154444, https://doi.org/10.1016/j.jallcom.2020.154444.

[2] B. Grushko, D. Holland-Moritz, R. Wittmann, G. Wilde, Transition between periodic and quasiperiodic structures in Al–Ni–Co, J. Alloy. Compd. 280 (1998) 215–230, https://doi.org/10.1016/S0925-8388(98)00722-1.

[3] L. Meshi, S. Samuha, D. Kapush, D. Pavlyuchkov, B. Grushko, New complex intermetallic in the Al–Rh–Ru alloy system, J. Alloy. Compd. 509 (2011) 6551–6555, https://doi.org/10.1016/j.jallcom.2011.03.108.

[4] B. Grushko, D. Kapush, T.Ya Velikanova, S. Samuha, L. Meshi, An investigation of the Al–Rh–Ru phase diagram above 50 at% Al, J. Alloy. Compd. 509 (2011) 8018–8021, https://doi.org/10.1016/j.jallcom.2011.05.074.

[5] S. Samuha, E. Mugnaioli, B. Grushko, U. Kolb, L. Meshi, Atomic structure solution of the complex quasicrystal approximant Al_{77} Rh_{15} Ru_8 from electron diffraction

data, Acta Crystallogr. Sect. B Struct. Sci. Cryst. Eng. Mater. 70 (2014) 999–1005, https://doi.org/10.1107/S2052520614022033.

[6] B. Grushko, A study of the Al-rich region of the Al–Fe–Ir alloy system, J. Alloy. Metall. Syst. 4 (2023) 100040, https://doi.org/10.1016/j.jalmes.2023.100040.

[7] S. Balanetskyy, B. Grushko, T.Ya Velikanova, K. Urban, An investigation of the Al–Pd–Fe phase diagram between 50 and 100 at% Al: phase equilibria at 750 °C, J. Alloy. Compd. 376 (2004) 158–164, https://doi.org/10.1016/j.jallcom.2004.01.023.

[8] M. Gemmi, E. Mugnaioli, T.E. Gorelik, U. Kolb, L. Palatinus, P. Boullay, S. Hovmöller, J.P. Abrahams, 3D Electron Diffraction: The Nanocrystallography Revolution, ACS Cent. Sci. 5 (2019) 1315–1329, https://doi.org/10.1021/acscentsci.9b00394.

[9] M. Gemmi, A.E. Lanza, 3D electron diffraction techniques, Acta Crystallogr. Sect. B Struct. Sci. Cryst. Eng. Mater. 75 (2019) 495–504, https://doi.org/10.1107/S2052520619007510.

[10] U. Kolb, T. Gorelik, C. Kübel, M.T. Otten, D. Hubert, Towards automated diffraction tomography: Part I—Data acquisition, Ultramicroscopy 107 (2007) 507–513, https://doi.org/10.1016/j.ultramic.2006.10.007.

[11] P.A. Midgley, A.S. Eggeman, Precession electron diffraction – a topical review, IUCrJ 2 (2015) 126–136, https://doi.org/10.1107/S2052252514022283.

[12] R. Vincent, P.A. Midgley, Double conical beam-rocking system for measurement of integrated electron diffraction intensities, Ultramicroscopy 53 (1994) 271–282, https://doi.org/10.1016/0304-3991(94)90039-6.

[13] E.F. Rauch, J. Portillo, S. Nicolopoulos, D. Bultreys, S. Rouvimov, P. Moeck, Automated nanocrystal orientation and phase mapping in the transmission electron microscope on the basis of precession electron diffraction, Z. Kristal 225 (2010) 103–109, https://doi.org/10.1524/zkri.2010.1205.

[14] L. Meshi, S. Samuha, Characterization of Atomic Structures of Nanosized Intermetallic Compounds Using Electron Diffraction Methods, Adv. Mater. 30 (2018) 1706704, https://doi.org/10.1002/adma.201706704.

[15] L. Palatinus, P. Brázda, M. Jelínek, J. Hrdá, G. Steciuk, M. Klementová, Specifics of the data processing of precession electron diffraction tomography data and their implementation in the program *PETS2.0*, Acta Crystallogr. Sect. B Struct. Sci. Cryst. Eng. Mater. 75 (2019) 512–522, https://doi.org/10.1107/S2052520619007534.

[16] S. Ranganathan, A. Subramaniam, Orthorhombic rational approximants for decagonal quasicrystals, Bull. Mater. Sci. 26 (2003) 627–631, https://doi.org/10.1007/BF02704327.

[17] B. Grushko, J. Gwóźdź, M. Yurechko, Investigation of the Al–Cu–Rh phase diagram in the vicinity of the decagonal phase, J. Alloy. Compd. 305 (2000) 219–224, https://doi.org/10.1016/S0925-8388(00)00754-4.

[18] D. Singh, S. Hovmöller, Structure Analysis of Quasicrystal Approximants by Rotation Electron Diffraction (RED), in: D. Singh, S. Condurache-Bota (Eds.), Electron Crystallogr, IntechOpen, 2020, https://doi.org/10.5772/intechopen.91372.

[19] A. Colin Cameron, F.A.G. Windmeijer, An R-squared measure of goodness of fit for some common nonlinear regression models, J. Econ. 77 (1997) 329–342, https://doi.org/10.1016/S0304-4076(96)01818-0.

[20] A.R. Denton, N.W. Ashcroft, Vegard's law, Phys. Rev. A 43 (1991) 3161–3164, https://doi.org/10.1103/PhysRevA.43.3161.

[21] T. Hahn, Int. Tables Crystallogr. 1 (1983) 182.

[22] E. Abe, Atomic-Scale Characterization of Nanostructured Metallic Materials by HAADF/Z-contrast STEM, Mater. Trans. 44 (2003) 2035–2041, https://doi.org/10.2320/matertrans.44.2035.

[23] K. Sohlberg, T.J. Pennycook, W. Zhou, S.J. Pennycook, Insights into the physical chemistry of materials from advances in HAADF-STEM, Phys. Chem. Chem. Phys. 17 (2015) 3982–4006, https://doi.org/10.1039/C4CP04232H.

[24] M.C. Burla, R. Caliandro, B. Carrozzini, G.L. Cascarano, C. Cuocci, C. Giacovazzo, M. Mallamo, A. Mazzone, G. Polidori, Crystal structure determination and refinement *via SIR2014*, J. Appl. Crystallogr 48 (2015) 306–309, https://doi.org/10.1107/S1600576715001132.

[25] V. Petříček, M. Dušek, L. Palatinus, Crystallographic Computing System JANA2006: General features, Z. Kristal. - Cryst. Mater. 229 (2014) 345–352, https://doi.org/10.1515/zkri-2014-1737.

[26] C. Liu, K. Kitahara, A. Ishikawa, T. Hiroto, A. Singh, E. Fujita, Y. Katsura, Y. Inada, R. Tamura, K. Kimura, R. Yoshida, Quasicrystals predicted and discovered by machine learning, Phys. Rev. Mater. 7 (2023) 093805, https://doi.org/10.1103/PhysRevMaterials.7.093805.

[27] D. Pavlyuchkov, B. Grushko, T.Ya Velikanova, An investigation of the high-Al part of the Al–Pd–Ru phase diagram at 790–900°C, J. Alloy. Compd. 469 (2009) 146–151, https://doi.org/10.1016/j.jallcom.2008.01.138.

[28] K. Kitahara, H. Takakura, Y. Iwasaki, K. Kimura, Phase Equilibria in Aluminium–Ruthenium–Silicon System near 1200 Kelvin, Mater. Trans. 65 (2024) 18–26, https://doi.org/10.2320/matertrans.MT-M2023128.

[29] B. Grushko, T. Velikanova, Formation of quasiperiodic and related periodic intermetallics in alloy systems of aluminum with transition metals, Calphad 31 (2007) 217–232, https://doi.org/10.1016/j.calphad.2006.12.002.

[30] Z. Zhang, H. Tian, Y.H. Chen, W. Sun, Special planar defects in the structural complex metallic alloys of Al-Pd-Mn and Al-Ni-Rh, Int. J. Mater. Res. 97 (2006) 1001–1007.

[31] M. Boudard, Structural themes in approximant and decagonal quasicrystalline phases in Al based alloys, J. Alloy. Compd. 495 (2010) 365–371, https://doi.org/10.1016/j.jallcom.2009.10.063.